be precisely measured and engineered experimentally. In comparison, a 2D SO coupling via a tripod system (*7*, *24*, *27*) or ring-coupling scheme (*25*) corresponds to pseudospins defined by superpositions of multiple hyperfine levels with superposition coefficients being spatially dependent. This conceptual difference manifests the advantages of the present realization for future broad studies of SO effects and interacting physics. Furthermore, owing to the realization in the optical lattice, the present 2D SO coupling can bring about much richer physics than a pure 2D Rashba correspondence. In the s-band regime, the present Bloch Hamiltonian describes a quantum anomalous Hall model driven by SO coupling, which cannot be exactly realized in solid-state materials. Thus, even in the single-particle regime, our realization leads to nontrivial topological bands, whereas a single-particle 2D Rashba system is topologically trivial. Moreover, even richer physics can be obtained if considering the higher-band (e.g., p-band) regimes.

Many experimental studies—including the measurement of topological Hall effects, Berry phase mechanism, and k-space monopole—can be performed on the basis of the present realization. On the other hand, with the high controllability of the present realization, the SO interaction can be readily switched on and off and can be adjusted between 1D and 2D limits. This may lead to rich quench spin dynamics in the optical lattice with nontrivial band topology. Moreover, with the present SO coupling in the optical lattice, one may explore states of matter [such as SO-coupled Mott insulators with interacting bosons (*35*, *36*)] that have no analog in solids.

Furthermore, the present optical Raman lattice scheme is generic and can be immediately applied to fermion systems (e.g., ^{40}K), in which case, the quantum anomalous Hall effect in the single-particle regime and topological superfluid (*28*) or novel magnetic phases (*37*) in the interacting regimes will be especially noteworthy. In particular, the topological superfluid phase is highly sought after because it hosts Majorana quasiparticles, which obey non-Abelian statistics (*38*) and have attracted attention in both condensed matter and cold atom physics (*5*). Finally, although the present study is focused on a 2D lattice system, generalizing our scheme to 3D optical lattices may lead to the realization of topological phases in 3D systems, including the Weyl topological semimetals (*39*, *40*).

REFERENCES AND NOTES

1. M. Z. Hasan, C. L. Kane, *Rev. Mod. Phys.* **82**, 3045–3067 (2010).
2. X.-L. Qi, S.-C. Zhang, *Rev. Mod. Phys.* **83**, 1057–1110 (2011).
3. N. Read, D. Green, *Phys. Rev. B* **61**, 10267–10297 (2000).
4. A. Y. Kitaev, *Phys. Uspekhi* **44**, 131–136 (2001).
5. F. Wilczek, *Nat. Phys.* **5**, 614–618 (2009).
6. J. Alicea, *Rep. Prog. Phys.* **75**, 076501 (2012).
7. J. Ruseckas, G. Juzeliūnas, P. Öhberg, M. Fleischhauer, *Phys. Rev. Lett.* **95**, 010404 (2005).
8. K. Osterloh, M. Baig, L. Santos, P. Zoller, M. Lewenstein, *Phys. Rev. Lett.* **95**, 010403 (2005).
9. X.-J. Liu, M. F. Borunda, X. Liu, J. Sinova, *Phys. Rev. Lett.* **102**, 046402 (2009).
10. Y.-J. Lin, K. Jiménez-García, I. B. Spielman, *Nature* **471**, 83–86 (2011).
11. J.-Y. Zhang *et al.*, *Phys. Rev. Lett.* **109**, 115301 (2012).
12. P. Wang *et al.*, *Phys. Rev. Lett.* **109**, 095301 (2012).
13. L. W. Cheuk *et al.*, *Phys. Rev. Lett.* **109**, 095302 (2012).
14. K. Jiménez-García *et al.*, *Phys. Rev. Lett.* **108**, 225303 (2012).
15. C. Wang, C. Gao, C.-M. Jian, H. Zhai, *Phys. Rev. Lett.* **105**, 160403 (2010).
16. C.-J. Wu, I. Mondragon-Shem, X.-F. Zhou, *Chin. Phys. Lett.* **28**, 097102 (2011).
17. T.-L. Ho, S. Zhang, *Phys. Rev. Lett.* **107**, 150403 (2011).
18. S.-C. Ji *et al.*, *Nat. Phys.* **10**, 314–320 (2014).
19. V. Galitski, I. B. Spielman, *Nature* **494**, 49–54 (2013).
20. T. F. J. Poon, X.-J. Liu, *Phys. Rev. A* **93**, 063420 (2016).
21. N. Goldman, G. Juzeliūnas, P. Öhberg, I. B. Spielman, *Rep. Prog. Phys.* **77**, 126401 (2014).
22. C. Zhang, S. Tewari, R. M. Lutchyn, S. Das Sarma, *Phys. Rev. Lett.* **101**, 160401 (2008).
23. M. Sato, Y. Takahashi, S. Fujimoto, *Phys. Rev. Lett.* **103**, 020401 (2009).
24. C. Zhang, *Phys. Rev. A* **82**, 021607(R) (2010).
25. D. L. Campbell, G. Juzeliūnas, I. B. Spielman, *Phys. Rev. A* **84**, 025602 (2011).
26. N. R. Cooper, *Phys. Rev. Lett.* **106**, 175301 (2011).
27. L. Huang *et al.*, *Nat. Phys.* **12**, 540–544 (2016).
28. X.-J. Liu, K. T. Law, T. K. Ng, *Phys. Rev. Lett.* **112**, 086401 (2014).
29. M. Aidelsburger *et al.*, *Phys. Rev. Lett.* **111**, 185301 (2013).
30. H. Miyake, G. A. Siviloglou, C. J. Kennedy, W. C. Burton, W. Ketterle, *Phys. Rev. Lett.* **111**, 185302 (2013).
31. M. Aidelsburger *et al.*, *Nat. Phys.* **11**, 162–166 (2015).
32. See supplementary materials for more details about model realization, SO coupling, nontrivial topological bands, band topological measurement, and estimation of heating.
33. X.-J. Liu, K. T. Law, T. K. Ng, P. A. Lee, *Phys. Rev. Lett.* **111**, 120402 (2013).
34. S.-C. Ji *et al.*, *Phys. Rev. Lett.* **114**, 105301 (2015).
35. Z. Cai, X. Zhou, C. Wu, *Phys. Rev. A* **85**, 061605(R) (2012).
36. W.-S. Cole, S. Zhang, A. Paramekanti, N. Trivedi, *Phys. Rev. Lett.* **109**, 085302 (2012).
37. J. Radić, A. Di Ciolo, K. Sun, V. Galitski, *Phys. Rev. Lett.* **109**, 085303 (2012).
38. D. A. Ivanov, *Phys. Rev. Lett.* **86**, 268–271 (2001).
39. S.-Y. Xu *et al.*, *Science* **349**, 613–617 (2015).
40. H. Weng, C. Fang, Z. Fang, B. A. Bernevig, X. Dai, *Phys. Rev. X* **5**, 011029 (2015).

ACKNOWLEDGMENTS

We thank J. Ho, T.-F. J. Poon, and G.-B. Jo for helpful discussions. This work has been supported by the Ministry of Science and Technology of China (under grants 2016YFA0301601 and 2016YFA0301604), National Natural Science Foundation of China, the CAS, the National Fundamental Research Program (under grant 2013CB922001), Fundamental Research Funds for the Central Universities (under grants 2030020028 and 2340000034), and Peking University Initiative Scientific Research Program. X.-J.L. acknowledges support from the National Natural Science Foundation of China (grant 11574008). X.-J.L. and L.Z. are also supported by the Thousand-Young-Talent Program of China.

SUPPLEMENTARY MATERIALS

www.sciencemag.org/content/354/6308/83/suppl/DC1
Supplementary Text
Figs. S1 to S6
References (*41*, *42*)

11 March 2016; accepted 12 September 2016
10.1126/science.aaf6689

REPORTS

GEOPHYSICS

Localized seismic deformation in the upper mantle revealed by dense seismic arrays

Asaf Inbal,* Jean Paul Ampuero, Robert W. Clayton

Seismicity along continental transform faults is usually confined to the upper half of the crust, but the Newport-Inglewood fault (NIF), a major fault traversing the Los Angeles basin, is seismically active down to the upper mantle. We use seismic array analysis to illuminate the seismogenic root of the NIF beneath Long Beach, California, and identify seismicity in an actively deforming localized zone penetrating the lithospheric mantle. Deep earthquakes, which are spatially correlated with geochemical evidence of a fluid pathway from the mantle, as well as with a sharp vertical offset in the lithosphere-asthenosphere boundary, exhibit narrow size distribution and weak temporal clustering. We attribute these characteristics to a transition from strong to weak interaction regimes in a system of seismic asperities embedded in a ductile fault zone matrix.

Earthquakes occurring along transform plate boundaries are generally confined to the upper portions of the crust, with upper mantle deformation being predominantly aseismic (*1*). Seismological investigations of active faulting at lower crustal depths are limited by highly attenuated signals whose level barely exceeds the noise at Earth's surface, and by the sparseness of regional seismic networks. Consequently, important physical parameters characterizing the transition from brittle fracture to ductile flow at the base of the seismogenic zone are generally very poorly determined (*2*).

Because seismic tomography usually cannot resolve features whose spatial extent is less than about 10 km in the mid-lower crust (*3*–*5*), the

Seismological Laboratory, California Institute of Technology, Pasadena, CA 91125, USA.
***Corresponding author. Email: ainbal@gps.caltech.edu**

occurrence of localized shear at those depths is largely inferred from geological observation of ancient shear zones, where tectonic deformation can be accommodated within a region whose thickness does not exceed 2 km (*6*). The presence of fault-generated melt in the form of pseudotachylytes injected into exposed mylonites, and the inferred subsequent ductile deformation of the two, indicate that seismic slip may occur within largely aseismic deep shear zones (*7*). This is often interpreted as resulting from ruptures that nucleate at shallow depth but penetrate into the deep ductile region enabled, for example, by thermal weakening mechanisms (*8*). Here, in contrast, we present evidence of deep seismicity that nucleates at lower crustal to upper mantle conditions.

The Newport-Inglewood fault (NIF), which hosts many deep earthquakes (*9*), is unusual in that it does not display the strong compression, relatively low heat flow, or strong topographical relief associated with deep faults in southern California (*10*–*12*). Moreover, given the local geothermal gradient [~32°C/km (*13*)], deep NIF seismicity nucleates at depths where typical continental crustal rocks are expected to deform in a ductile manner. To understand the long-term mode of seismic deformation along this fault, we examined a relocated earthquake catalog from the Southern California Seismic Network (SCSN) (*14*). We observed a systematic variation in the spatial pattern of microseismicity along the NIF strike, which we attribute to a transition in faulting style. Earthquake epicenters are tightly clustered on en echelon strike-slip faults northwest of Long Beach (LB) but do not follow the mapped trace of the NIF to the southeast of LB (Fig. 1A). From northwest to southeast, earthquake density decreases and maximum earthquake depth, which we define as the depth above which 95% of seismicity occurs, increases from 10 to 17 km. Along the same section, Mohorovičić discontinuity (Moho) depth decreases by about 5 km (Fig. 1C). The opposite trends of focal and Moho depths represent an unusual case in which the increase in seismogenic depth is anticorrelated with crustal thickness (*12*). Finding such deep events is surprising on a slow [0.5 to 1 mm/year (*15*)] tectonic fault such as the NIF. Ductile flow laws predict that the depth of the brittle-ductile transition increases with strain rate (*16*, *17*). This should result in a shallower transition along the NIF compared with that along the faster San Andreas fault [~2 cm/year (*18*)], assuming similar pressure and friction coefficient on these two faults. Moreover, if we make the common assumption that seismicity rate correlates with strain rate, then the observed 50-fold reduction in earthquake rate recorded by the SCSN from northwest of Rosecrans to LB (Fig. 1A) should have been accompanied by resolvably shallower seismicity. To improve our understanding of the spatial distribution of anomalous NIF seismicity, we examined earthquake properties in two NIF segments that host the deepest events reported in the regional catalog.

Our study is based on earthquake detection from continuous, simultaneous analysis of thousands of seismic channels from two dense arrays

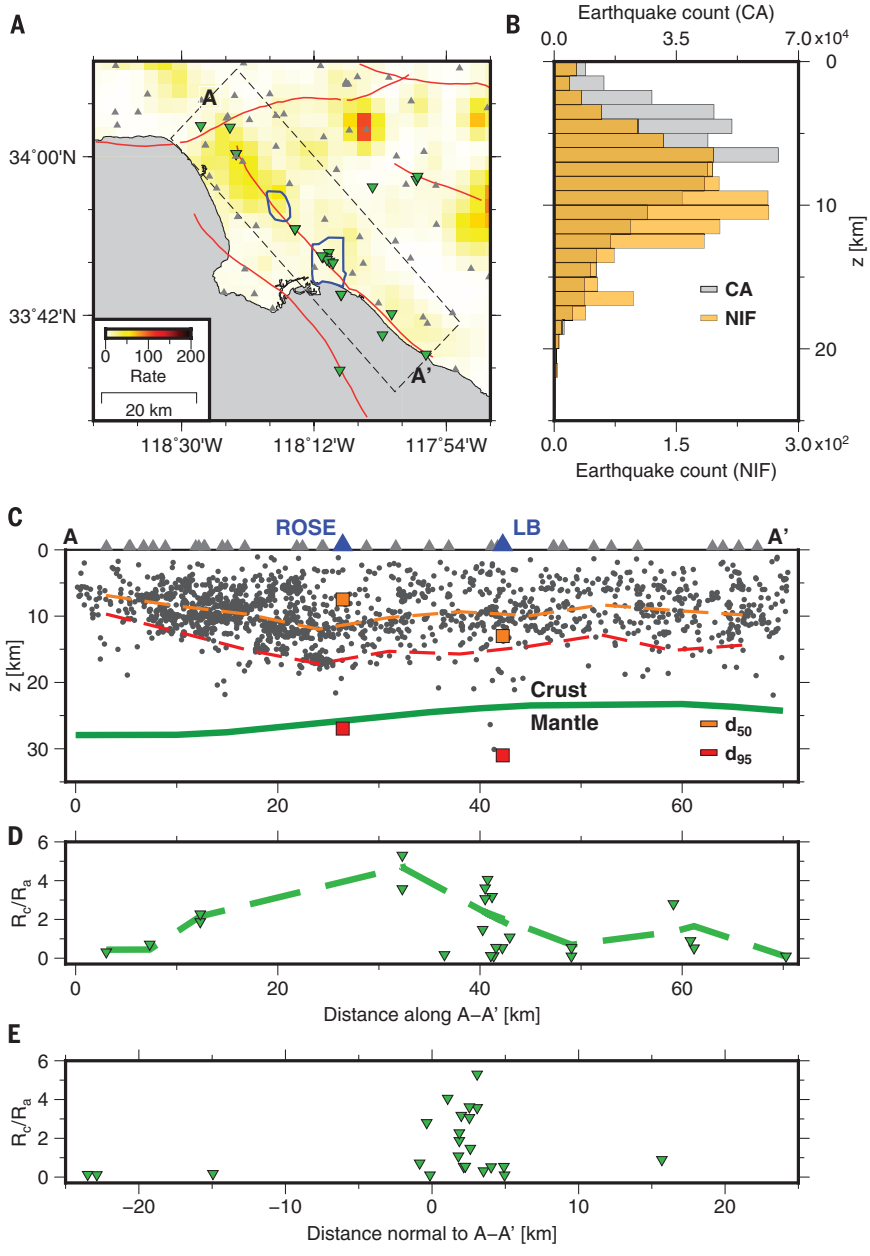

Fig. 1. Earthquake density, seismicity, and helium ratios. This figure shows the spatial distribution of seismicity that occurred between 1980 and 2011 and was recorded by the Southern California Seismic California (SCSN) (*14*), as well as helium ratios (^{3}He/^{4}He) in the LA basin, which were measured and corrected for air contamination by Boles *et al.* (*25*). (**A**) Earthquake density as a function of location. We used the color bar labeled "Rate" to indicate the spatially smoothed number of events over a 30-year period, binned in 9-km^2 squares. The locations of helium measurements, seismic stations, and dense seismic arrays are denoted by green inverted triangles, gray triangles, and blue polygons, respectively. The dashed rectangle indicates the region from which we extracted the earthquakes used to construct panels (B) and (C). Red curves denote the surface trace of active faults. (**B**) SCSN catalog seismicity depth distribution along the Newport-Inglewood fault (NIF) and in southern California (CA). *z* is the depth below sea level. (**C**) Depths of NIF seismicity and the Moho as function of location along line A-A′ in (A). The Moho (*45*, *46*) is indicated by the green curve. The depths (d) above which 50 and 95% of the earthquakes occur in the SCSN- and back-projection–derived catalogs are indicated by the orange and red dashed curves and squares, respectively. Gray triangles represent the projection of SCSN seismic stations onto the line A-A′; blue triangles denote the arrays. ROSE indicates the Rosecrans Array and LB denotes the Long Beach Array. (**D**) Helium ratios within the area enclosed by the dashed rectangle in (A), as a function of distance along A-A′. The dashed curve indicates the polynomial best fit to the observations. Green inverted triangles are the same as in (A). R_a is the ^{3}He/^{4}He ratio in air; R_c is the same for the crust. (**E**) Helium ratios as a function of distance normal to A-A′.

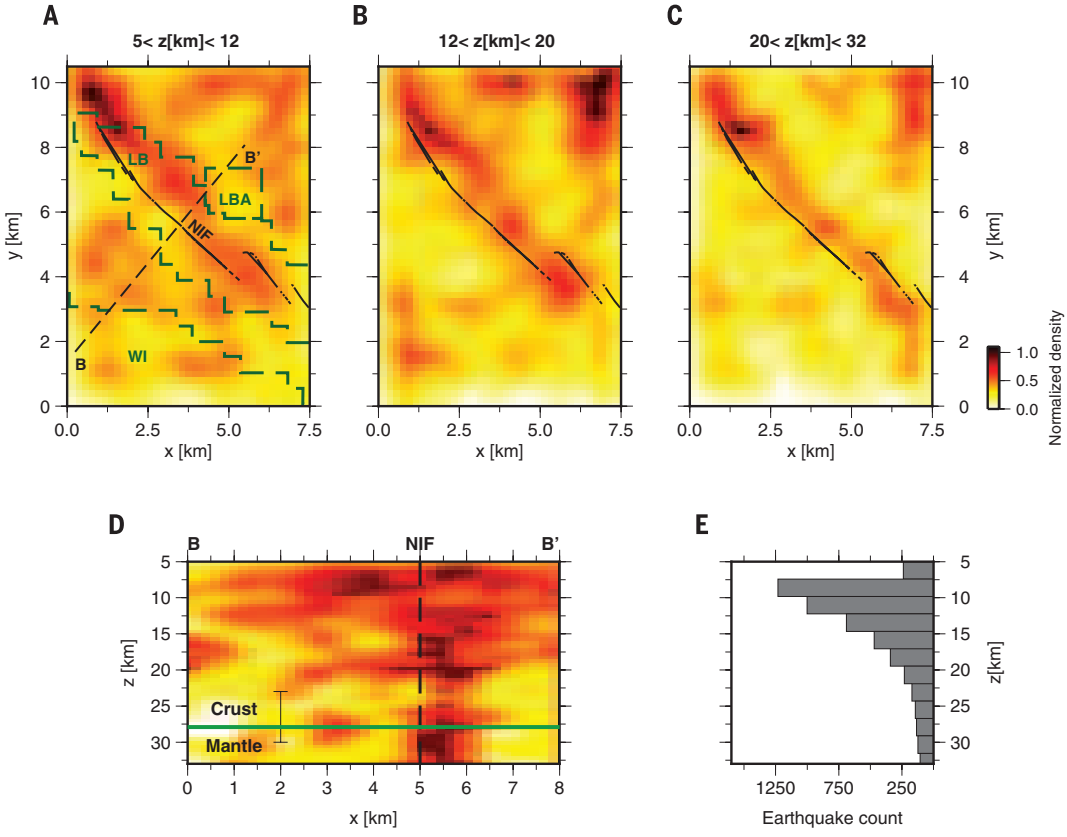

Fig. 2. Spatial distribution of earthquake density derived from a catalog spanning 93 nights of the LB Array data set. (**A** to **C**) Map view of event density in the following depth ranges: (A) 5 to 12 km, (B) 12 to 20 km, and (C) 20 to 32 km. Densities in each panel were normalized by their maximum value. Areas with intense seismicity are shown in orange and red; areas devoid of seismicity appear in yellow and white. The NIF surface trace and the local oilfields are denoted by black and green dashed lines, respectively. LB, Long Beach oilfield; LBA, Long Beach Airport oilfield; WI, Wilmington oilfield. (**D**) Vertical cross section showing event density along the B-B′ line in (A). We normalized the counts in each 2-km depth bin by their maxima. The Moho depth (*47*) is indicated by a green curve, and the uncertainty on this estimate was determined using previously published results (*26*, *38*, *48*). (**E**) Seismicity depth distribution in the LB Array data set.

(Fig. 1A and figs. S2 and S4 to S7) (*9*, *19*). We used the 5200-sensor 7-km–by–10-km LB Array and the 2600-sensor 5-km–by–5-km Rosecrans Array to compile catalogs with 6 and 1 month of data, respectively. The arrays contain 100-m-spaced, 10-Hz vertical geophones sampling at 500 Hz. We analyzed only nighttime data (6 p.m. to 5 a.m. Pacific time) to mitigate false detections. We used parallel computing on graphical processing units to process 80 terabytes, equivalent to about 80 years of waveform data from the Global Seismographic Network (*20*). The location uncertainties we estimated through synthetic tests (*21*) are 1 and 3 km in the horizontal and vertical directions, respectively, for events with moment magnitude (M_w) > 1.5 occurring below 27 km, but less than 1 km at shallower depths (fig. S1).

Our catalog illuminates a transition from diffuse seismic deformation in the upper crust to localized deformation in the lithospheric mantle. Shallow seismicity (<12 km) in LB is diffuse and uncorrelated with the mapped fault trace or with the nearby oilfield (Fig. 2A). To the southwest of the main NIF strand, we identify a northwest–north-northwest striking segment that is mostly active between 12 and 20 km but contains sparse seismicity outside this depth range. A second structure is located to the northeast. Below 20 km, this zone is very seismically active, but the location near the edge of the array prevents us from resolving its geometry in detail.

With increasing depth, seismicity progressively concentrates beneath the mapped trace of the NIF, and the width of the seismically active zone decreases (Fig. 2, A to C). Below ~20 km, seismicity localizes onto a 1-km-wide area that is located directly beneath the mapped trace of the NIF. The vertical cross section (Fig. 2D) clearly shows that the fault dip below 15 km is near vertical and that it retains this geometry in the upper mantle. In particular, our observations do not support a previous suggestion that the NIF is truncated at shallow depths by an active detachment fault (*22*). Accounting for location uncertainties in our catalog, the deformation zone illuminated by deep LB seismicity is no more than 2 km wide, consistent with several exhumed mylonite shear zones (*6*). We also find that deep seismicity (>20 km) accounts for, at most, 10 to 20% of the cumulative long-term moment rate accommodated by the fault, assuming a slip rate of 0.5 mm/year (*15*). On the basis of these results, we conclude that aseismic, viscous flow accommodates most of the deformation in the lower crust.

The spatial distribution of deep seismicity varies along the NIF strike. Seismicity in Rosecrans occurs along four or five strands that form a 5-km-wide fault zone, which is active down to about 15 km but contains few events below that depth. Unlike the LB segment, these strands appear to dip at up to 70° to the northeast (fig. S3). Multiple en echelon strike-slip faults are generally observed at shallower depths along that section (*23*), and our study confirms that these structures are active at larger depths. If the Rosecrans catalog is representative of the long-term deformation along that segment, then the scarcity of deep seismicity suggests that the zone of deep, localized seismic deformation extends no more than 15 km along the NIF strike to the northwest of LB.

Independent evidence compatible with deep faulting comes from recent measurements of the $^3He/^4He$ ratio, a primary indicator of mantle-derived phases within the crust (*24*), in deep boreholes in the Los Angeles (LA) basin (*25*) (Fig. 1, A, D, and E). In this basin, ^3He enrichment is more than twice as high as it is along the much more tectonically active San Andreas fault. The observed along-strike trend in the fraction of mantle-derived helium is well correlated with the seismicity depths in the regional catalog. They both first increase toward the southeast, then decrease somewhat and flatten southeast of LB (Fig. 1, C and D). Further evidence of the deep root of the NIF comes from the seismic imaging of a sharp vertical offset in the lithosphere-asthenosphere boundary (*26*), which extends to a depth of about 90 km beneath

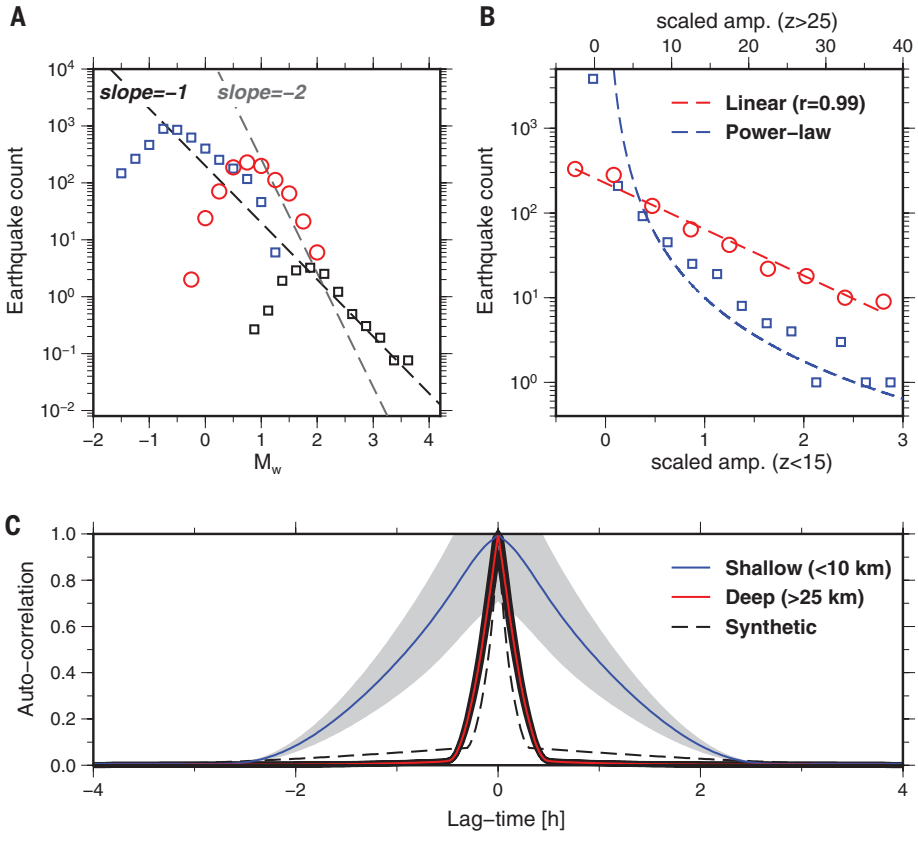

Fig. 3. Temporal analysis and earthquake size distribution in Long Beach. (**A**) Distribution of earthquake magnitudes. The blue squares and red circles denote shallow (<15 km) and deep (>25 km) events, respectively. The black squares are for the SCSN catalog and are normalized according to the LB Array spatiotemporal coverage. The slopes of black and gray dashed lines are equal to –1 and –2, respectively. (**B**) Distribution of earthquake signal amplitudes, which we define as the maximum of the downward-continued, migrated stack in a 5-s window containing the event, scaled by the maximum of the synthetic stack computed for a collocated source with M_w = 1. The best-fitting exponential model, which appears linear in this semi-logarithmic scale, is indicated by the red curve. The blue curve shows a power law. *r*, correlation coefficient. (**C**) Autocorrelation as a function of lag-time between earthquake rate time series for shallow (<10 km) and deep (>25 km) clusters. The blue and red curves indicate the average values for 112 shallow and 52 deep clusters, respectively. The gray shaded area denotes the 1σ uncertainties. The black dashed curve represent a synthetic earthquake catalog with a random, Poissonian distribution of earthquake occurrences.

the zone of deep seismicity and anomalous ^{3}He enrichment. We suggest that the narrow deformation zone hosting deep seismicity beneath LB acts as a major conduit for fluid transfer between the upper mantle and the crust. These fluids, in turn, could provide a source of high pressures that extend the depth of seismic deformation.

The along-depth variation in the spatial distribution of NIF seismicity is most likely due to a rheological transition, which we expected to manifest itself as a resolvable change in the statistics of the catalog. To test this hypothesis, we analyzed the temporal clustering of LB seismicity. Because our spatial resolution is limited by location uncertainties that are likely larger than the rupture dimensions of the earthquakes we imaged, we focused on aspects of the population's temporal and size distributions, which varied on scales of several hundred meters.

We can investigate the degree of earthquake interaction using the ratio between the number of small and large earthquakes, commonly characterized by the *b* value ($b = -d\log_{10}(N)/dM_w$, where *N* is the number of earthquakes of magnitude larger than M_w). In most tectonic environments, *b* values vary between 0.8 and 1.5 and decrease with increasing deviatoric stress (*27*). Larger *b* values are associated with an increase in ductility and a reduction of fault strength, both in the lab (*28*) and on natural faults (*29*). Recent observations of low-frequency earthquakes (LFEs), whose collective failure results in tectonic tremors, suggest that their numbers fall off rapidly with increasing size (estimated from tremor amplitudes). Those studies suggest that LFE numbers are better described by an exponential distribution (*30*–*32*) or a very steep power law (*33*). The rapid fall-off in LFE numbers with increasing size is similar to deep NIF seismicity (*9*). However, unlike other areas, the NIF catalog captures a depth-dependent transition in earthquake properties (Fig. 3, A and B). The distribution of shallow (<15 km) earthquakes in the 6-month period is consistent with that of the 30 years spanning SCSN catalog. Our analysis closes a gap between the LB and SCSN magnitude-frequency distributions between M_w = 1 and 2 in our 3-week catalog (*9*).

Spatiotemporal clustering is ubiquitous in earthquake catalogs and manifests most notably in the form of mainshock-aftershock sequences. We can model seismic activity as a random Poissonian process because it decorrelates at large distances or long time intervals. Our previous analysis of 3 weeks of LB seismicity (*9*) demonstrated Omori-type temporal clustering at interevent distances of up to 2 km. To determine whether this behavior is depth-dependent, we analyzed the temporal autocorrelation functions of the spatially smoothed earthquake rates at different depth ranges (*21*). We found that deep earthquake occurrence shows weak temporal correlation and resembles a random Poissonian process (Fig. 3C). This indicates diminished earthquake interactions at these depths.

Models of lithospheric strength may explain deep NIF seismicity while incorporating constrains on lower crustal rheology (*17*). However, relevant parameters such as temperature, grain size, lithology, and water content are generally poorly constrained. One possibility is that lateral as well as vertical compositional changes in the lower crust will promote brittleness within ductile, generally aseismic regions. A line of evidence supports the existence of considerable heterogeneity in material properties at lower crustal to upper mantle depth beneath the NIF. These include the observation of a sharp offset in the lithosphere-asthenosphere boundary extending to 90 km depth beneath the NIF (*26*); a 10-km jump in the Moho, 16 km to the west of the NIF (*34*); travel-time tomography showing a fast, possibly mafic body starting at ~18 km beneath the LA basin (*35*); magnetic profiles suggesting that the NIF is the southern boundary of an ultramafic body (*36*); and along-strike variations in the orientation of the principal stress axes (*37*), the distribution of mantle helium (*25*), and near-surface (*23*) and deep faulting styles. Structural factors may also assist slip localization. The fabric of foliated mica schists, which are thought to be distributed at lower crustal depths beneath California (*38*, *39*), possibly contains discrete surfaces accommodating seismic slip. Unstable frictional sliding of mafic rock has been observed in lab experiments (*40*, *41*) and in the field. (*42*, *43*). This behavior may be further encouraged in the presence of fluids, either by reducing the effective normal stress or by promoting strain localization in narrow shear bands (*44*), perhaps akin to the localized deformation zone we imaged beneath LB (Fig. 2C).

The rheological transition has profound implications on the degree of fault localization, relaxation mechanisms, and earthquake scaling properties. We can reconcile these observations with a conceptual framework in which deep deformation is predominately accommodated by ductile flow but interspersed by seismogenic asperities. Seismic rupture nucleated in a brittle asperity can penetrate into the surrounding region, up to a certain distance

that generally depends on the asperity size and stress drop and on the resistance of the matrix. This effective radius R_e controls the range of interaction between asperities. The ratio between R_e and the interasperity distance Δ determines the ability of asperities to break together in seismic events, despite the intervening creep, and thus influences the statistics of the earthquake catalog. When R_e/Δ is large, ruptures can involve multiple asperities. This strong interaction regime potentially leads to a scale-free, power-law earthquake size distribution (Fig. 3A) and temporal clustering (Fig. 3C), as observed at shallow depths. When R_e/Δ is small, asperities tend to break in isolation. In this weak interaction regime, seismicity is temporally uncorrelated and, if asperities have a characteristic size, the earthquake size distribution is scale-bound, as observed in the deep NIF beneath LB. A systematic decrease of R_e/Δ with increasing depth may result from several processes, which are not necessarily independent. One possibility is a rheological control: R_e may decrease with depth due to increasing velocity strengthening of the creeping matrix or decreasing stress drop within the asperities. Another possibility is a geometrical (or structural) control: At larger depths, the range of asperity sizes (and, hence, of R_e) may be narrower or Δ may be larger (e.g., due to lithological variations).

REFERENCES AND NOTES

1. A. Maggi, J. Jackson, D. McKenzie, K. Priestley, *Geology* **28**, 495–498 (2000).
2. R. Bürgmann, G. Dresen, *Annu. Rev. Earth Planet. Sci.* **36**, 531–567 (2008).
3. C. Thurber *et al.*, *Bull. Seismol. Soc. Am.* **96**, S38–S49 (2006).
4. M. Kahraman *et al.*, *Earth Planet. Sci. Lett.* **430**, 129–139 (2015).
5. J. H. Shaw *et al.*, *Earth Planet. Sci. Lett.* **415**, 1–15 (2015).
6. R. J. Norris, A. F. Cooper, *J. Struct. Geol.* **25**, 2141–2157 (2003).
7. J. C. White, *J. Struct. Geol.* **38**, 11–20 (2012).
8. J. R. Rice, *J. Geophys. Res.* **111**, B05311 (2006).
9. A. Inbal, R. Clayton, J.-P. Ampuero, *Geophys. Res. Lett.* **42**, 6314–6323 (2015).
10. A. S. Bryant, L. M. Jones, *J. Geophys. Res.* **97**, 437–447 (1992).
11. H. Magistrale, *Geophys. Res. Lett.* **29**, 87-1–87-4 (2002).
12. E. Hauksson, *Geophys. J. Int.* **186**, 82–98 (2011).
13. L. C. Price, M. J. Pawlewicz, T. A. Daws, "Organic metamorphism in the California petroleum basins: Chapter A, Rock-Eval and vitrinite reflectance" (U.S. Geological Survey Bulletin 2174-A, 1999).
14. E. Hauksson, W. Yang, P. M. Shearer, *Bull. Seismol. Soc. Am.* **102**, 2239–2244 (2012).
15. L. B. Grant, J. T. Waggoner, T. K. Rockwell, C. vonStein, *Bull. Seismol. Soc. Am.* **87**, 277–293 (1997).
16. D. L. Kohlstedt, B. Evans, S. J. Mackwell, *J. Geophys. Res.* **100**, 17587–17602 (1995).
17. G. Hirth, N. M. Beeler, *Geology* **43**, 223–226 (2015).
18. E. O. Lindsey, Y. Fialko, *J. Geophys. Res.* **118**, 689–697 (2013).
19. J. Gazdag, *Geophys.* **43**, 1342–1351 (1978).
20. IRIS, Incorporated Research Institutions for Seismology; www.iris.edu/hq.
21. Materials and methods are available as supplementary materials on *Science* Online.
22. J. Crouch, J. Suppe, *Geol. Soc. Am. Bull.* **105**, 1415–1434 (1993).
23. T. L. Wright, "Structural geology and tectonic evolution of the Los Angeles Basin, California," in American Association of Petroleum Geologists Memoir 52, K. T. Biddle, Ed. (1991), pp. 35–134.
24. B. M. Kennedy *et al.*, *Science* **278**, 1278–1281 (1997).
25. J. R. Boles, G. Garven, H. Camacho, J. E. Lupton, *Geochem. Geophys. Geosyst.* **16**, 2364–2381 (2015).
26. V. Lekic, S. W. French, K. M. Fischer, *Science* **334**, 783–787 (2011).
27. C. H. Scholz, *Geophys. Res. Lett.* **42**, 1399–1402 (2015).
28. C. H. Scholz, *Bull. Seismol. Soc. Am.* **58**, 399–415 (1968).
29. M. Spada, T. Tormann, S. Wiemer, B. Enescu, *Geophys. Res. Lett.* **40**, 709–714 (2013).
30. T. Watanabe, Y. Hiramatsu, K. Obara, *Geophys. Res. Lett.* **34**, L07305 (2007).
31. D. R. Shelly, J. L. Hardebeck, *Geophys. Res. Lett.* **37**, L14301 (2010).
32. J. R. Sweet, K. C. Creager, H. Houston, *Geochem. Geophys. Geosyst.* **15**, 3713–3721 (2014).
33. M. G. Bostock, A. M. Thomas, G. Savard, L. Chuang, A. M. Rubin, *J. Geophys. Res.* **120**, 6329–6350 (2015).
34. B. Schmandt, R. W. Clayton, *J. Geophys. Res.* **118**, 5320–5338 (2013).
35. E. Hauksson, *J. Geophys. Res.* **105**, 13875–13903 (2000).
36. T. Romanyuk, W. D. Mooney, S. Detweiler, *J. Geodyn.* **43**, 274–307 (2007).
37. E. Hauksson, *Bull. Seismol. Soc. Am.* **77**, 539–561 (1987).
38. R. Porter, G. Zandt, N. McQuarrie, *Lithosphere* **3**, 201–220 (2011).
39. P. Audet, *J. Geophys. Res.* **120**, 3527–3543 (2015).
40. D. S. H. King, C. Marone, *J. Geophys. Res.* **117**, B12203 (2012).
41. E. K. Mitchell, Y. Fialko, K. M. Brown, *Geochem. Geophys. Geosyst.* **16**, 4006–4020 (2015).
42. T. Ueda, M. Obata, G. Di Toro, K. Kanagawa, K. Ozawa, *Geology* **36**, 607–610 (2008).
43. A. K. Matysiak, C. A. Trepmann, *Tectonophys.* **530–531**, 111–127 (2012).
44. A. J. Getsinger, G. Hirth, H. Stunitz, E. T. Goergen, *Geochem. Geophys. Geosyst.* **14**, 2247–2264 (2013).
45. J. H. Shaw *et al.*, *Earth Planet. Sci. Lett.* **415**, 1–15 (2015).
46. C. Tape, A. Plesch, J. H. Shaw, H. Gilbert, *Seismol. Res. Lett.* **83**, 728–735 (2012).
47. Y. Ma, R. Clayton, *Geophys. J. Int.* **206**, 1645–1651 (2016).
48. Z. Yan, R. W. Clayton, *J. Geophys. Res.* **112**, B05311 (2007).

ACKNOWLEDGMENTS

We thank Signal Hill Petroleum and NodalSeismic for granting us permission to use the Long Beach Array data, and we thank Breitburn Energy and LA Seismic for permission to use the Rosecrans Array data. We acknowledge J. P. Avouac, R. Bürgmann, Y. Ma, and W. Frank for helpful discussions. This research was supported by NSF awards EAR-1214912 and EAR-1520081 and by the Terrestrial Hazard Observation and Reporting Center at Caltech. The seismic data are property of Signal Hill Petroleum and Breitburn Energy. Data are available for noncommercial use through a license agreement with the data owners that includes but is not limited to a nondistribution agreement. Please contact the authors for additional information.

SUPPLEMENTARY MATERIALS

www.sciencemag.org/content/354/6308/88/suppl/DC1
Materials and Methods
Figs. S1 to S7
References (*49*, *50*)

23 December 2015; accepted 31 August 2016
10.1126/science.aaf1370

SOLAR CELLS

Quantum dot–induced phase stabilization of α-$CsPbI_3$ perovskite for high-efficiency photovoltaics

Abhishek Swarnkar,[1,2] Ashley R. Marshall,[1,3] Erin M. Sanehira,[1,4] Boris D. Chernomordik,[1] David T. Moore,[1] Jeffrey A. Christians,[1] Tamoghna Chakrabarti,[5] Joseph M. Luther[1]*

We show nanoscale phase stabilization of $CsPbI_3$ quantum dots (QDs) to low temperatures that can be used as the active component of efficient optoelectronic devices. $CsPbI_3$ is an all-inorganic analog to the hybrid organic cation halide perovskites, but the cubic phase of bulk $CsPbI_3$ (α-$CsPbI_3$)—the variant with desirable band gap—is only stable at high temperatures. We describe the formation of α-$CsPbI_3$ QD films that are phase-stable for months in ambient air. The films exhibit long-range electronic transport and were used to fabricate colloidal perovskite QD photovoltaic cells with an open-circuit voltage of 1.23 volts and efficiency of 10.77%. These devices also function as light-emitting diodes with low turn-on voltage and tunable emission.

Hybrid organic-inorganic halide perovskites, with the common formulation ABX_3 (where A is an organic cation, B is commonly Pb^{2+}, and X is a halide), were first applied to photovoltaics (PVs) as methylammonium lead triiodide ($CH_3NH_3PbI_3$) in 2009 (*1*). Perovskite PV devices processed from solution inks now convert >22% of incident sunlight into electricity, which is on par with the best thin-film chalcogenide and silicon devices, but durability of the semiconductor presents a major technical hurdle to commercialization. Under environmental stress, $CH_3NH_3PbI_3$ dissociates into PbI_2 and CH_3NH_3I, the latter of which is volatile (*2*).

Thus, an all-inorganic structure without a volatile organic component is highly desired. The all-inorganic Pb-halide perovskite with the most appropriate band gap E_g for PV applications is cubic (α) $CsPbI_3$ (E_g = 1.73 eV) because geometrical constraints of the perovskite structure require a large +1 A-site cation, and Cs^+ is the most feasible. However, below 320°C, the orthorhombic (δ) phase (E_g = 2.82 eV) is thermodynamically

[1]Chemical and Materials Science, National Renewable Energy Laboratory (NREL), Golden, CO 80401, USA. [2]Department of Chemistry, Indian Institute of Science Education and Research (IISER), Pune 411008, India. [3]Department of Chemistry and Biochemistry, University of Colorado, Boulder, CO 80309, USA. [4]Department of Electrical Engineering, University of Washington, Seattle, WA 98195, USA. [5]Metallurgical and Materials Engineering, Colorado School of Mines, Golden, CO 80401, USA.
***Corresponding author. Email: joey.luther@nrel.gov**

Localized seismic deformation in the upper mantle revealed by dense seismic arrays

Asaf Inbal, Jean Paul Ampuero and Robert W. Clayton

Science **354** (6308), 88-92.
DOI: 10.1126/science.aaf1370

Earthquakes get a more flexible source

Earth's surface deforms in part as a result of ruptures along brittle crustal faults that generate earthquakes. Understanding rock deformation in the ductile lower crust and mantle is challenging. Using the densest seismic arrays in the world, Inbal *et al.* have found an unexpected localization of seismicity at these depths under the Newport-Inglewood fault in southern California. The seismicity points to a type of earthquake that may help us understand how ductile deformation operates in this region of Earth.

Science, this issue p. 88